

## DRAG COEFFICIENT CHARACTERIZATION OF THE ORIGAMI MAGIC BALL

Guanyu Chen<sup>1</sup>, Dongsheng Chen<sup>1</sup>, Jessica Weakly<sup>1</sup>, Cynthia Sung<sup>1,\*</sup>

<sup>1</sup>University of Pennsylvania, Philadelphia, PA

### **ABSTRACT**

The drag coefficient plays a vital role in the design and optimization of robots that move through fluids. From aircraft to underwater vehicles, their geometries are specially engineered so that the drag coefficients are as low as possible to achieve energy-efficient performances. Origami magic balls are 3-dimensional reconfigurable geometries composed of repeated simple waterbomb units. Their volumes can change as their geometries vary and we have used this concept in a recent underwater robot design. This paper characterizes the drag coefficient of an origami magic ball in a wind tunnel. Through dimensional analysis, the scenario where the robot swims underwater is equivalently transferred to the situation when it is in the wind tunnel. With experiments, we have collected and analyzed the drag force data. It is concluded that the drag coefficient of the magic ball increases from around 0.64 to 1.26 as it transforms from a slim ellipsoidal shape to an oblate spherical shape. Additionally, three different magic balls produce increases in the drag coefficient of between 57% and 86% on average compared to the smooth geometries of the same size and aspect ratio. The results will be useful in future designs of robots using waterbomb origami in fluidic environments.

**Keywords:** Origami, magic ball, drag coefficient

### **NOMENCLATURE**

$C_d$	Drag coefficient
$D$	Drag [N]
$A_a$	Cross sectional area of samples [ $\text{m}^2$ ]
$v_a$	Wind speed [m/s]
$v_w$	Swimming speed of the robot [m/s]
$\rho_a$	Density of air at 25 °C [1.184 kg/m <sup>3</sup> ]
$Re$	Reynolds number
$l_a$	Length of the scaled-down samples [mm]
$l_w$	Length of the regular-sized magic ball [mm]
$\nu_a$	Kinematic viscosity of air at 25 °C [1.56 × 10 <sup>-5</sup> m <sup>2</sup> /s]

$\nu_w$	Kinematic viscosity of water at 25 °C [8.92 × 10 <sup>-7</sup> m <sup>2</sup> /s]
$\alpha$	Scale factor
$d_a$	Diameter of the scaled-down samples [mm]
$d_w$	Diameter of the regular-sized samples [mm]
$m$	Number of rows of waterbomb units on the magic ball pattern
$n$	Number of columns of waterbomb units on the magic ball pattern
$s_a$	Side length of waterbomb units on the scaled-down magic ball pattern [mm]
$s_w$	Side length of waterbomb units on the regular-sized magic ball pattern [mm]
$f_{ptl}$	Factor to convert the length in pixel to the real length in mm
$L_p$	A set that stores the length of the regular-sized magic ball in pixels
$W_p$	A set that stores the diameter values of the regular-sized magic ball in pixels
$P_v$	Pressure reading of Dwyer Mark II Manometer [inches of water]
$l_{wref}$	Reference length of the regular-sized magic balls [mm]
$l_{aref}$	Reference length of the scaled-down magic balls [mm]
$\Delta l$	Length displacement [mm]
$\alpha_c$	Corrected scale factor
$c_i$	Constant coefficients of the ellipse equation ( $i = 1, 2$ )
$d_c$	Diameter of the end caps of the samples [mm]
$l_{ca}$	Longitudinal length of each stripe during the polygonalization process of the ellipsoid fabrication [mm]
$l_e$	Distance from one end to a certain position along the length of the corresponding magic ball [mm]
$h_a$	Width of each stripe during the polygonalization process of the ellipsoid fabrication [mm]
$p$	Number of stripes during the polygonalization process of the ellipsoid fabrication
x, y	Coordinates in the Cartesian coordinate system

\*Corresponding author: crsung@seas.upenn.edu

## 1. INTRODUCTION

Origami-inspired fabrication approaches enable 3D structures to be constructed quickly and easily [1–5] by folding flat sheets of material. Besides the reconfigurability, origami robots can be easy to store, transport, and shape into and interact with an object’s surface due to their lightweight, thin thickness, and high flexibility [6]. The origami magic ball is one example of origami patterns that have been used in a number of robotic designs. The magic ball is composed of multiple repeated patterns called waterbomb units with a six-crease base [7] to form a revolved body. Once folded, it is able to continuously transform from an elongated “ellipsoidal” shape to a shorter “spherical” and even a flattened “wheel” shape. Because of its high transformability, the magic ball has been used in applications as varied as a deformable wheel [8], an origami swimmer [9], and a worm robot [10].

In previous work, we have taken advantage of the origami magic ball’s ability to change geometry and volume to design an underwater robot that generates jets to propel itself through the water [9]. The origami magic ball converts length change into volumetric change, enabling a simple actuation system that uses a DC motor and a single tendon to produce a jet. The swimmer draws in water slowly by contracting in length and expanding its magic ball body, and it then ejects the water very fast under the effect of the rubber band around it for propulsion. We constructed a proof-of-concept that demonstrated that the robot can swim untethered at a speed of 6.7 cm/s (0.2 body lengths/s). However, the design was unoptimized, and we expect that properties such as the drag, thrust, and resulting energy efficiency of the robot will be heavily influenced by the geometry of the body. Thus, in this work, we characterize the drag of the magic ball forming the robot’s body so that in the future, we can enhance the robot’s energy efficiency by modifying the pattern design of the magic ball skin and applying proper control methods.

The drag coefficient is a significant factor in the process of designing and developing robots that travel through air or water, such as UAVs [11], flying robots [12], and underwater robots [9]. In general, drag is the force opposing the forward motion of the robot, and thus reducing drag is key to maximizing a robot’s locomotive efficiency. Drag can be controlled using a number of factors, primarily the geometry of the vehicle. In [13], for example, the influence of the drag coefficient on the locomotion speed of the robotic fish was studied by adjusting the fin amplitude. The work in [14] proposed an energy prediction model based on drag coefficients and other energy-consumption-related components and demonstrated that this model was able to efficiently provide assistance in the analysis of the energy consumption characteristics of mobile robots. The work in [15] derived an inverse dynamics control law based on the air drag force and demonstrated the significance of considering the air drag force for lightweight higher-speed robots.

The drag coefficient of a variety of origami patterns has been characterized. Zhang et al. [16] have studied the aerodynamic drag of the Miura-ori in different deployable configurations. In [17], kirigami patterns have been incorporated into origami structures comprised of thin-film materials to build drone guards, and the drag of the structures has been measured to investigate the aerodynamic properties of the deformable structures. Cozmei et

al. [18] have explored the use of two novel origami designs, Worm and Dino, as active aerodynamic control surfaces based on drag values, and they found that the designs had excellent structural rigidity and folding characteristics under aerodynamic loading. Tolman et al. [19] have developed a deployable aerodynamic locomotive fairing based on thick origami and implemented a Computational Fluid Dynamics (CFD) simulation to demonstrate the drag reduction of the fairing. Marzin et al. [20] have discovered that shape reconfiguration through origami folding sets an upper limit on drag by focusing on a single waterbomb cell as a generic case. However, the drag coefficient of origami magic balls has not been characterized yet.

In this paper, we present an experimental drag coefficient characterization for origami magic balls, with a focus on the geometries and fluid conditions of interest for our swimming robot. We conduct load tests in a wind tunnel to evaluate the drag on the robot for a number of different geometries (including different resolutions and lengths of the magic ball), measured at the average speed at which the robot swims. The results demonstrate that the drag coefficient of the magic ball increases from 0.64 to 1.26 as it transforms from the ellipsoidal state to the spherical state, but the drag coefficient remains generally the same over different pattern resolutions. We also compared the magic ball to smooth ellipsoids of the same size and aspect ratio, showing that the magic ball produces an increase of 57–86% in drag coefficient compared to the smooth surfaces.

The rest of the paper is organized as follows. In Sect. 2, a brief overview of our robot and its relevant parameters are introduced. In Sect. 3, we discuss scaling laws and our strategy for wind tunnel tests. In Sect. 4, we introduce the experimental setup, the fabrication process of the magic ball samples and ellipsoid samples, and the experimental procedure. Then, we present and discuss the results of the drag and drag coefficient of the samples. In Sect. 5, we conclude and discuss limitations and future work.

## 2. ORIGAMI MAGIC BALL AND RELEVANT PARAMETERS

### 2.1 Overview of Origami Magic Ball

In this paper, we focus on the magic ball origami pattern. The magic ball is a tessellation of waterbomb units, as shown in Fig. 1 (left). The shape of the folded magic ball is influenced by three main parameters:  $m$ , the number of rows of units;  $n$ , the number of columns of units; and  $s_w$ , the side length of one unit. The pattern in Fig. 1 has 4 rows and 5 columns of units, so we call it a  $4 \times 5$  magic ball pattern.

After folding all the units and connecting the sides of the pattern, the magic ball pattern can be turned into a dimpled ellipsoid shape which is called the magic ball, shown in Fig. 1 (right). For convenience, the magic ball folded by  $m \times n$  magic ball pattern is called  $m \times 2n$  magic ball because one magic ball takes two magic ball patterns to fold [9]. The structure has the ability to continuously deform even after folding, converting lengthwise contraction into diameter expansion, and vice versa. We call the length of the folded magic ball  $l_w$  and the diameter at its equator  $d_w$ . Sect. 4.1 provides more information about the relationship between these two variables as the magic ball deforms.

In our previous work [9], we found that the ratio  $m/(2n) \approx 2/5$  can generally work well to produce a large volume change

without buckling. Thus, in this paper, we primarily focus on the  $4 \times 10$ ,  $5 \times 12$ , and  $6 \times 15$  magic balls, keeping the total surface of the balls constant.

## 2.2 Scaling the Ball for Drag Tests

Our full-scale origami swimmer [9] uses two  $4 \times 5$  magic ball patterns with  $s_w = 88$  mm, resulting in a folded structure with lengths between  $l_w = 230$  mm and  $l_w = 170$  mm and diameters approximately between  $d_w = 190$  mm and  $d_w = 260$  mm. However, this structure would be too large for our wind tunnel, and thus we scale our magic balls down in size.

Let  $\alpha = 0.5$  be the geometric scale factor used for our experimental tests. Our drag measurements were then conducted on magic balls with unit length  $s_a = \alpha s_w$  compared to the original swimmer. Since the 3D geometry of the folded ball is fully captured by its resolution  $m$  and  $n$ , its unit length  $s_w$ , and its folded length  $l_w$ , if the length of the folded structure is also scaled accordingly, then the geometry of the scaled ball should be equivalent. We use the subscript  $a$  to denote the dimensions of the scaled ball; that is,  $l_a$  is the length of the scaled-down magic ball, and  $d_a$  is its diameter. To ensure the shape consistency between the regular-sized magic balls and scaled-down ones, the length-diameter profile of the regular-sized ones is discovered in Sect. 4.1.

## 3. THEORY OF CALCULATING DRAG COEFFICIENT USING CONVERTED WIND SPEED

The drag coefficient is a dimensionless number used by engineers to model the effects of shape and flow conditions on drag [21]. If an object moves with a velocity of  $v_a$  in a flow that has a density of  $\rho_a$ , and if the frontal area of the object that is perpendicular to the flow is  $A_a$  and the drag force acting on the object is  $D$ , then the drag coefficient  $C_d$  can be calculated using Eq. (1).

$$C_d = \frac{2D}{\rho_a A_a v_a^2} \quad (1)$$

The drag coefficient of an object can be affected by the Reynolds number, the Mach number, the surface roughness of the material used to fabricate the object, the sample geometry [21], and the Froude number [22]. The Reynolds number is the ratio of inertial forces to viscous forces. When the Reynolds number is low, the drag coefficient is typically high since the laminar flow is dominated. When the Reynolds number is high, the drag coefficient is typically low due to the prevalence of turbulent flow. The Mach number is the ratio of the velocity of an object to the sound speed. At a low Mach number, the drag coefficient is not significantly affected by changes in Mach number. Surface roughness refers to the deviations or irregularities in the surface texture of a material. At a low Reynolds number, a high surface roughness can lead to a high drag coefficient since the flow is very sensitive to the disturbance caused by the friction between the object and the fluid. For the shape of an object, streamlined shapes can have a lower drag coefficient since they can minimize the formation of vortices. On the contrary, blunt shapes can have a higher drag coefficient since more turbulence is likely to be generated. The Froude number expresses the ratio of inertial forces to gravitational forces in a flow. According to [22], if the depth of an ellipsoid is four times

longer than its diameter, the effect of the Froude number can be ignored.

In our experiment, we measure the drag force of the scaled-down samples in a wind tunnel due to the limited size of the wind tunnel. Then, Eq. (1) is used to calculate the drag coefficient of our samples. The parameter  $\rho_a$  in our experiment is the density of air,  $A_a$  is the cross-sectional area of our scaled-down samples that is perpendicular to the wind,  $v_a$  is the wind speed in the wind tunnel, and  $D$  is the drag force acting on our samples. The cross-sectional area of the scaled-down magic balls  $A_a$  can be calculated by approximating the section as a circle with a diameter of  $d_a$ , so  $A_a \approx \pi d_a^2 / 4$ . Among these parameters,  $\rho_a$  at  $25^\circ C$  is  $1.184 \text{ kg/m}^3$ , and  $D$  is obtained through drag measurement. Hence, it is necessary to figure out  $v_a$  to further calculate the drag coefficient.

Since the robot is intended to swim underwater but the drag is measured in the air, the swimming speed  $v_w$  is converted to the wind speed  $v_a$  with dimensional analysis to reflect the real scenario. To ensure the consistency of the drag coefficient in different fluids, the influencing factors of the drag coefficient should be well controlled. For our robot, the maximum swimming speed of our robot is approximately  $0.067 \text{ m/s}$  [9], which is far slower than the sonic speed. Thus, the Mach number is not considered. As an estimate, the swimming speed  $v_w$  is chosen to be  $0.1 \text{ m/s}$  since it has the same order of magnitude as  $0.067 \text{ m/s}$ . Since the working conditions can be far below the water surface the most of time, the Froude number is not considered in the speed conversion, either. Furthermore, since the samples for the drag measurement are fabricated using the same material and folded into the same shape as the robot that swims underwater, the influence of the surface roughness and shape can be controlled. Therefore, only the Reynolds number  $Re$  needs to be considered.

$$\begin{aligned} Re &= \frac{v_a l_a}{\nu_a} = \frac{v_w l_w}{\nu_w} \\ v_a &= \frac{v_a l_w}{v_w l_a} v_w = \frac{v_a v_w}{v_w \alpha} \end{aligned} \quad (2)$$

where  $\nu_w$  and  $\nu_a$  are the kinematic viscosity of water and air, respectively,  $l_w$  and  $l_a$  are the characteristic lengths of the regular-sized robot and the scaled-down samples, respectively, and  $\alpha = l_a/l_w$  is the geometric scale factor. For a scale factor of  $\alpha = 0.5$ , and the wind speed required for our experiments can be obtained as  $v_a = 3.5 \text{ m/s}$ .

## 4. EXPERIMENTS ON ORIGAMI MAGIC BALLS AND ELLIPSOIDS

### 4.1 Extraction of Length-Diameter Profile

To ensure the shape consistency between the regular-sized robot and the scaled-down samples, the length-diameter ratios of the three regular-sized magic balls ( $4 \times 10$ ,  $5 \times 12$ , and  $6 \times 15$  magic balls) are extracted using computer vision. Four red markers are attached to the top, bottom, left, and right sides of the regular-sized magic balls, as shown in Fig. 2. Rubber bands are fixed around the rows above and below the equator to replicate the working conditions of the real robot. Then, the magic balls are compressed once using an MTS machine (Criterion C43.504 with  $50 \text{ kN}$  load cell) with a compression displacement of  $60 \text{ mm}$  and

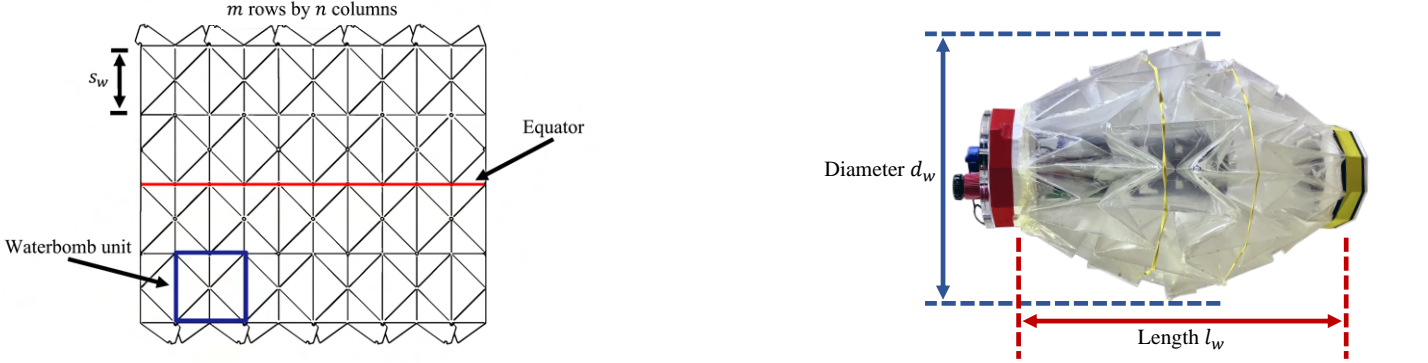


**FIGURE 1: THE ORIGAMI MAGIC BALL IS A WATERBOMB TESSELLATION (LEFT) WITH  $m$  ROWS AND  $n$  COLUMNS OF SQUARE WATERBOMB UNITS. WHEN THE LEFT AND RIGHT SIDES OF THE PATTERN ARE GLUED TOGETHER, THE PATTERN FOLDS INTO A TUBULAR SHAPE (RIGHT) OF LENGTH  $l_w$  AND OUTER DIAMETER  $d_w$ . THE MAGIC BALL ON THE RIGHT HAS 4 ROWS AND 10 COLUMNS, AND IT IS FABRICATED BY GLUING TWO  $4 \times 5$  MAGIC BALL PATTERNS (LEFT) TOGETHER. IMAGES MODIFIED FROM [9].**

a compression rate of 1 mm/s after it is pre-compressed 10 times. The final compression is recorded by a Nikon digital camera D3400 with a resolution of 1080p and a frame rate of 60 fps. The video then is processed with the hue filter in Python and the central pixel positions of the four markers are determined in each frame using *opencv*. Finally, the length of the magic ball in pixels is calculated by the pixel positions of the top and bottom markers, while the diameter of the magic ball in pixels is calculated by the pixel positions of the left and right markers. Since the magic balls are compressed by 60 mm, the factor that converts the pixel length to the real length in mm,  $f_{ptl}$  can be obtained using

$$f_{ptl} = \frac{60 \text{ mm}}{\text{Max}\{L_p\} - \text{Min}\{L_p\}} \quad (3)$$

where  $L_p$  is a set that stores all lengths in pixels in all frames,  $\text{Max}\{L_p\}$  and  $\text{Min}\{L_p\}$  are the maximum and the minimum value in  $L_p$ , respectively, and  $f_{ptl}$  is the real length in mm per pixel. Thus, the real length of the magic ball,  $l_w$  in all frames can be calculated by  $f_{ptl}L_p$ . Similarly, the real diameter of the magic ball,  $d_w$  in all frames can be calculated by  $f_{ptl}W_p$  where  $W_p$  is a set that stores all diameters of the magic ball in pixels in all frames. Figure 3 shows the results of this process, along with a third-order polynomial fit. These values are used in the following fabrication process.

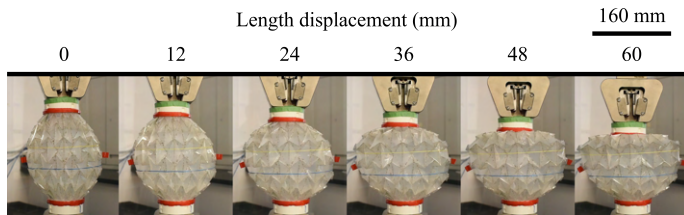


**FIGURE 2:  $6 \times 15$  MAGIC BALL WITH MARKERS AND RUBBER BANDS IN THE MTS MACHINE**

#### 4.2 Fabrication of Samples

**4.2.1 Magic Ball Samples.** The scaled-down waterbomb samples are fabricated out of 0.076-mm-thick PET (polyethylene

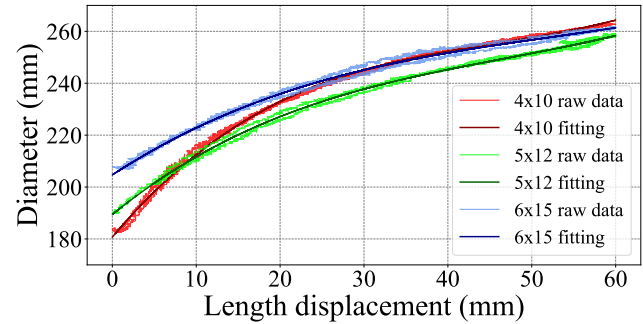


**FIGURE 3: DIAMETER VS. LENGTH DISPLACEMENT FOR REGULAR-SIZED MAGIC BALLS (FULL LENGTH: 234.46 MM FOR  $4 \times 10$  MAGIC BALL, 249.11 MM FOR  $5 \times 12$  MAGIC BALL, AND 231.64 MM FOR  $6 \times 15$  MAGIC BALL)**

terephthalate) sheets, as shown in the first row of Fig. 4. The patterns are cut into two pieces on a PLS 4.75 (Universal Laser System) flatbed laser cutter. The boundaries of the patterns are directly cut and the folds are perforated at 9 dots per cm. The two sides of the two pieces of patterns are taped together with 3M 1522 tape and the overlapping triangles on the top and bottom of the pattern shown in Fig. 1 (left) are sealed using 3M 467MP tape, after which the patterns are folded manually into a magic ball.

The regular-sized magic balls can be compressed by 60 mm from the initial state, so the length displacements of the scaled-down samples used in the experiment are 0, 6, 12, 18, 24, and 30 mm. When the length displacement is 0 mm, the samples are in the ellipsoidal state or initial state, and they are in the spherical state when the displacement is 30 mm. The resulting geometries for the samples are shown in Fig. 5. Due to fabrication inconsistencies, the length of the scaled-down samples is slightly shorter than half of the length of the actual regular-sized ones by up to 4 mm. To ensure their shape consistency as their lengths decrease from their individual reference lengths (when the length displacement is zero), we control the length displacement instead of the length. The reference lengths of the  $4 \times 10$ ,  $5 \times 12$ , and

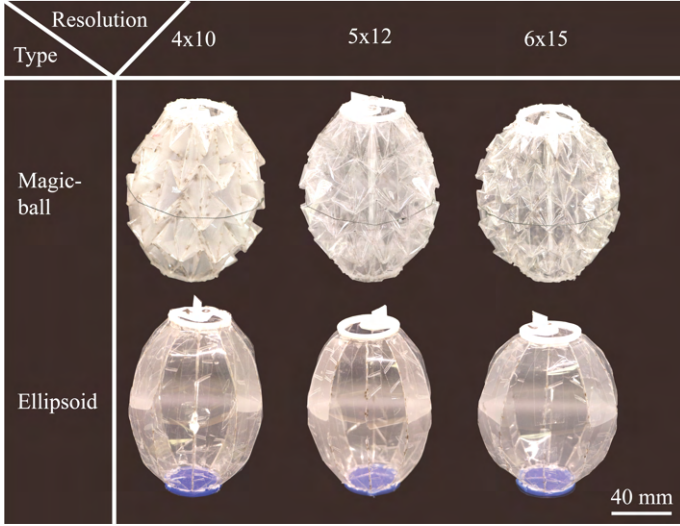
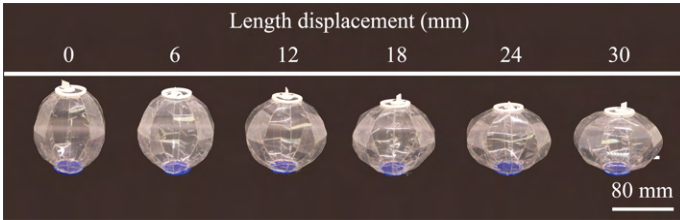


FIGURE 4: EXPERIMENTAL SAMPLES IN ELLIPSOIDAL STATE



(a) Magic ball samples

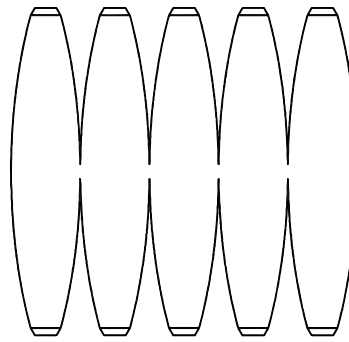


(b) Ellipsoid samples

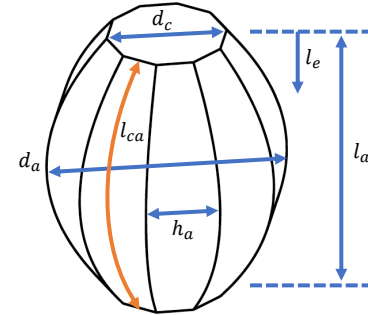
FIGURE 5: STATES OF SAMPLES TO BE TESTED (ELLIPSOIDAL STATE ON THE LEFT AND SPHERICAL STATE ON THE RIGHT)

6 × 15 regular-sized magic balls from computer vision,  $l_{wref}$  are 234.46 mm, 249.11 mm, and 231.64 mm, while the lengths of the corresponding scaled-down magic balls,  $l_{aref}$  are 113 mm, 109 mm, and 106 mm. Note that the length reported here is the length of the magic ball without considering end caps. The reference length obtained from computer vision is slightly longer than the actual length of the regular-sized magic balls, but their length-diameter ratios are verified to be typically the same as each other by taking a few states during the transformation process of the regular-sized magic ball since the diameter obtained from computer vision is also larger. Therefore, we used a corrected scale factor  $\alpha_c = l_{aref}/l_{wref}$  to convert the diameter obtained from computer vision to the desired diameter of the scaled-down samples.

The samples are fixed between two caps, which we use to control the length and fix the sample to the load measurement setup. The front cap is laser-cut from a 3.175-mm-thick acrylic



(a) Pattern used to fold polygonized ellipsoid. Two patterns are glued together horizontally to form a single ellipsoid.



(b) Geometric parameters of the ellipsoid

FIGURE 6: DIAGRAM OF THE POLYGONIZED ELLIPSOID AND THE RELATED PARAMETERS

board. The back cap is fabricated by 3D printing with PLA. Two holes on the extrusion of the back cap are used to mount the samples on the beam of the experimental setup using bolts and nuts as shown in Fig. 7b. Since the thickness of the material is not scaled down along with the geometry, it is possible that the deformation of the magic ball as it is compressed is not exactly the same as the regular-sized version. To find the corresponding diameter  $d_a$  of the scaled-down samples, we scale the diameters of the regular-sized magic balls obtained in Sect. 4.1 when the length displacement  $\Delta l$  is 0, 12, 24, 36, 48, and 60 mm, respectively. Thus, the diameter  $d_a$  can be obtained by  $d_a = \alpha_c d_w$ . Then, a fishing line loop is used to constrain the diameter of the sample to the required diameter to match the regular-sized sample. The fishing line loop is fabricated by cutting a section of the fishing line to a length of  $d_a$  and attaching two ends with super glue. The length displacement of the sample is adjusted by adding or removing 6-mm-long standoffs inside the sample between the two end caps.

**4.2.2 Ellipsoidal Samples.** To investigate the influence of the complex surface geometry formed by waterbomb units of the magic balls on the drag coefficient, ellipsoids with the same material, size, and length-diameter relationship as the magic balls are also fabricated. For each length and resolution of the magic ball sample, an ellipsoid is constructed to match the sample's length and diameter. The ellipsoid is made by polygonizing the surface of an ellipsoid with two flat ends into ten stripes along

the major axis, as shown in Fig. 6a, since it is difficult to directly fold a sheet into an ellipsoid. Figure 6b shows the geometric parameters of the polygonized ellipsoid. To design the proper shape of each stripe, the profile of the width of the stripes  $h_a$  over the longitudinal length of the stripes  $l_{ca}$  is derived below. Assume that the equation of the elliptic sectional shape of the ellipsoid obtained by cutting vertically along the diameter of the cap  $d_c$  in the 2D (x-y) Cartesian coordinate system is:

$$\frac{x^2}{c_1^2} + \frac{y^2}{c_2^2} = 1 \quad (4)$$

with boundary constraints:

$$y(x=0) = \frac{d_a}{2} \quad y\left(x = \frac{l_a}{2}\right) = \frac{d_c}{2} \quad (5)$$

where  $c_1$  and  $c_2$  are constant coefficients of the ellipse equation,  $d_c$  is the diameter of the end cap, and the origin of the coordinate system is fixed at the center of the ellipse with the x-axis pointing downwards along the major axis and the y-axis pointing horizontally along the minor axis. Therefore, it can be calculated that  $c_1^2 = \frac{l_a^2}{4\left[1 - \left(\frac{d_c}{d_a}\right)^2\right]}$  and  $c_2^2 = \left(\frac{d_a}{2}\right)^2$ . The horizontal width of each strip  $h_a$  is obtained by:

$$h_a(l_e) = 2y\left(x = -\frac{l_a}{2} + l_e\right) \sin\left(\frac{\pi}{p}\right) \quad (6)$$

where  $l_e$  is the distance from one end to a certain position along the length of the corresponding magic ball  $l_a$ , and  $p$  is the number of strips to form the polygonized ellipsoid.

$$l_{ca}(l_e) = \int_{-\frac{l_a}{2}}^{-\frac{l_a}{2} + l_e} \sqrt{1 + \left[\frac{d}{dx} \left(c_2^2 - x^2 \frac{c_2^2}{c_1^2}\right)^{\frac{1}{2}} \cos\left(\frac{\pi}{p}\right)\right]^2} dx \quad (7)$$

where  $l_{ca}$  is the longitudinal length of each stripe. Finally,  $h_a$  and  $l_{ca}$  along  $l_a$  are calculated in MATLAB 2021A, and a fourth-order polynomial is used to couple these two parameters. Then, the pattern is drawn in SolidWorks 2022 using equation-driven curves.

The boundaries of the pattern are cut as solid lines on the PLS 4.75 (Universal Laser System) flatbed laser cutter. Then, the curved edges of the adjacent stripes are glued together using 3M 1522 tape in the same way as for the magic ball samples. The tape is affixed to the inner side of the ellipsoid to reduce the influence of wrinkles at the connection between two adjacent stripes. The ellipsoid samples fabricated are shown in the second row of Fig. 4, and their transformations are shown in Fig. 5b.

The front and end caps are the same as those used for the scaled-down magic balls. However, no fishing lines or standoffs are used for ellipsoids since they can self-support their shapes. Eighteen ellipsoids are made to correspond to the 6 states of the 3 different magic balls. The ellipsoid that corresponds to an  $m \times n$  magic ball is called  $m \times n$  ellipsoid in the following.

### 4.3 Setup Description

The AEROLAB Educational Wind Tunnel (EWT) shown in Fig. 7a is used in the experiment. A fan is located on one end of the wind tunnel, and it can take in air from the other end. There is a chamber in the middle where samples can be placed and tested shown in Fig. 7b. Next to the chamber is a console panel used to turn on or off the fan and adjust the wind speed. The wind speed can be obtained by reading the pressure change due to the flow ( $P_v$  in inches of water) using a Dwyer Mark II Manometer. Using the datasheet [23] and assuming a temperature of 25 °C and a pressure of 1 atm, the conversion to wind speed can be computed as

$$v_a = 20.4952\sqrt{P_v} \quad (8)$$

In order to measure the drag force, we use the load cell setup shown in Fig. 7c. The setup consists of a load cell assembly, a base, a circuit, and a beam for attaching the samples. We use two Sparkfun 10 kg load cells (SEN-13329) with an error of 0.05%FS, rigidly coupled to prevent friction via machined aluminum brackets. The vertical load cell is for drag measurements, while the horizontal one is for lift measurements (not used). The base consists of two 6.35-mm-thick acrylic plates sized to fit the opening at the top of the wind tunnel. A 3D-printed connector attaches the beam to the load cell. The beam has a length of 220 mm and a thickness of 1.6 mm, and it is manufactured by waterjet cutting a steel sheet. The two holes on the low end of the beam allow the samples to be mounted.

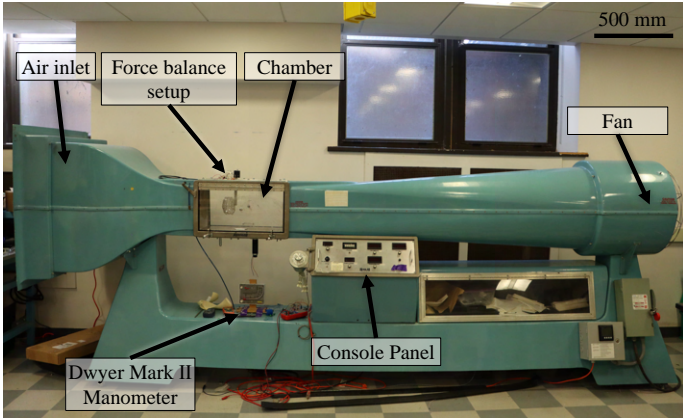
Load measurements are taken using an Arduino Uno and two Sparkfun HX711 load cell amplifiers (SEN-13879). The amplified load signal is uploaded from the Arduino Uno to a connected laptop using Serial communications over USB with a baud rate of 57600. After calibrating the load cells, we find the root mean square error (RMSE) of the load cell for drag is about 0.09 g. Since the samples are not made perfectly symmetrically, a lift force can be generated in the experiment. We manually exert some force in the lift direction as disturbance and find out the maximum error between the readings of the drag and the ground truth. The results in Table 1 show that even with a disturbance of 11.06 g in magnitude, the maximum error is only 0.38 g. Additionally, most of the maximum error lies within the range of 0.2 to 0.3 g with a disturbance smaller than 7 g in magnitude.

**TABLE 1: MAXIMUM ERROR OF DRAG WITH LIFT DISTURBANCE**

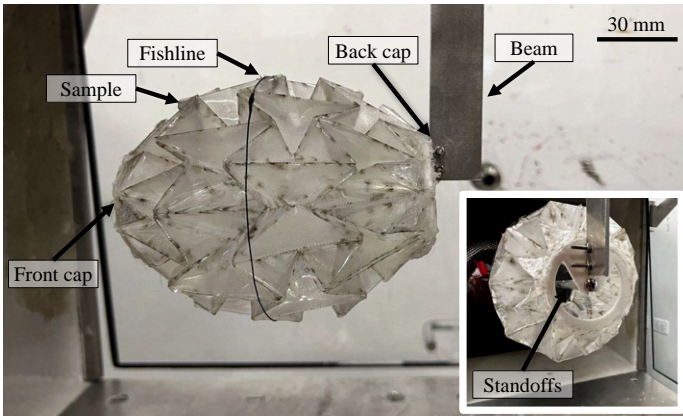
True drag (g)	Disturbance range (g)	Maximum error (g)
0.0	[−5.94, 7.00]	0.21
2.2	[−11.06, 7.98]	0.38
4.4	[−7.00, 5.73]	0.17
6.7	[−8.22, 4.64]	0.25
8.9	[−5.81, 4.32]	0.26
11.1	[−5.54, 4.37]	0.22
13.3	[−7.97, 5.10]	0.32

### 4.4 Experimental Procedures

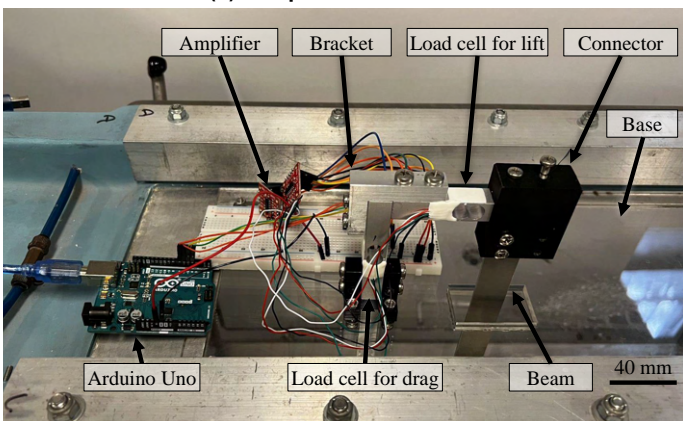
The force balance setup is placed upon the chamber of the wind tunnel with one end of the vertical beam inside the chamber.



(a) Wind tunnel



(b) Sample in the chamber



(c) Force balance setup

FIGURE 7: EXPERIMENTAL EQUIPMENT

The measurement process starts with a preliminary test to obtain the drag of only the beam and ensure that it is negligible compared with the drag of the samples. After connecting the Arduino Uno to a laptop, the data is collected from the load cells with the wind tunnel off. After the data readings stabilize, all prior data are cleared and only the incoming data are recorded for 40 s. The recorded data are saved before turning on the wind tunnel and adjusting the wind speed to 3.5 m/s. Then, the new data are recorded for 40 s. After that, the wind tunnel is turned off. This is the end of the preliminary test.

Following this procedure, data is collected for each of the samples. For each sample, the standoffs with full length are attached inside one of the scaled-down magic balls and the fishing line loop with the corresponding diameter is put around the sample. Then, the magic ball is attached to the vertical beam with bolts and nuts. At this time, the magic ball is in the ellipsoidal state. Similar to the base procedure, the data are recorded for 40 s and saved before turning on the fan and adjusting the wind speed to 3.5 m/s. The new data then are also recorded for 40 s. After that, the wind tunnel is turned off, and the magic ball is detached. This is one trial of the formal test for each magic ball sample. At the start of the next trial, one of the 6-mm-long standoffs is removed to compress the magic ball by 6 mm into a new state. The old fishing line loop is replaced by a new loop with a new diameter. After that, the sample with the new state is reattached to the beam. The above procedure except for the preliminary test is repeated for all magic ball samples with different states. Then, the procedure is repeated for the ellipsoid samples. The only difference between the test on the magic ball samples and ellipsoid samples is that no standoffs or fishing line loops are used in ellipsoid samples since we constructed a different ellipsoid to reflect the magic balls at every discrete state. Therefore, instead of removing standoffs to change the state, we directly attach different ellipsoids in each trial. In the experiment, all the data are collected only after the readings stabilize, which can be observed using a serial monitor.

#### 4.5 Results of Drag and Drag Coefficient and Analysis

The drag force for each trial is obtained by subtracting the mean of the data collected without wind from the 40-s data with the wind. The whole experimental procedure is implemented once for each trial. Fig. 8 shows the results. The dots represent the mean value of the drag force in each trial over the 40-s trial. The drag of the vertical beam is less than 0.1 g, which is negligible compared to the drag of the samples. In addition, since most of the lift disturbance in the experiment is less than 1 g and the maximum disturbance is only about 2.3 g in magnitude, the influence of the lift disturbance also has a negligible effect on the readings of the drag.

The drag of the magic balls and the ellipsoids both increase as they change from the ellipsoidal state to the spherical state. The magic ball patterns increase from around 2.9 g to 10.13 g, while the ellipsoidal samples increase from around 1.8 g to 5.93 g. The drag of magic balls in all states is thus about 1.36 to 2.33 times greater than that of the ellipsoids. For magic balls, the  $4 \times 10$  magic ball reaches the global highest drag of 11.91 g as it approaches the spherical state, while the  $5 \times 12$  magic

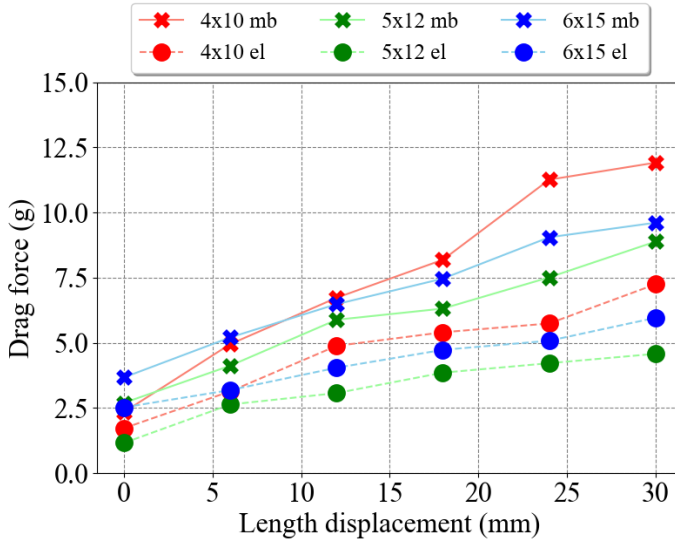


**FIGURE 8: COMPARISON OF DRAG.  $mb$ :=MAGIC BALL  $e/$ :=ELLIPSOID (MAXIMUM STANDARD DEVIATION IS 0.167 g FOR MAGIC BALLS, 0.117 g FOR ELLIPSOIDS)**

ball has the minimum value of drag in most of the states. In the spherical state, the drag of the  $4 \times 10$  magic ball is 1.34 times higher than that of the  $5 \times 12$  magic ball which is the smallest. In the ellipsoidal state, however, the  $4 \times 10$  magic ball has the minimum drag value and the  $6 \times 15$  magic ball has a maximum drag that is 1.57 times higher than that of the  $4 \times 10$  magic ball. For the ellipsoids, similarly, the  $4 \times 10$  ellipsoid has the highest drag of 7.25 g and the  $5 \times 12$  magic ball has the smallest drag in all states. In the spherical state, the drag of the  $4 \times 10$  ellipsoid is 1.58 times higher than that of the  $5 \times 12$  ellipsoid which is the smallest. In the ellipsoidal state, the  $6 \times 15$  magic ball has a maximum drag that is 2.18 times higher than that of the  $5 \times 12$  magic ball.

The drag coefficient, which has been obtained using Eq. (1) for all samples, is illustrated in Fig. 9. The drag coefficient of the magic balls with the three different pattern resolutions is generally similar for each state, varying by less than 37.3% between magic balls of different resolutions. In all cases of the magic balls, the drag coefficient increases from around 0.64 in the ellipsoidal state to slightly more than 1.26 in the spherical state. When the length displacement is 12, 18, and 30 mm, the drag of  $4 \times 10$  magic ball is the highest, but the drag coefficient is not the greatest. The reason is that the increase in the sectional area of the  $4 \times 10$  magic ball is large in these states, as shown in Fig. 10. Note that the sectional area of the magic balls and ellipsoids in the same state is identical. The drag coefficient of the ellipsoids rises from about 0.39 in the ellipsoidal state to 0.73 in the spherical state. The ratio of the change in the drag coefficient between the  $4 \times 10$ ,  $5 \times 12$ , and  $6 \times 15$  magic balls and the corresponding ellipsoids to the drag coefficient of the corresponding ellipsoids in each state are calculated, respectively. By taking the average of those ratios, we find that the complex surface geometry of the magic ball roughly leads to a 57%, 86%, and 61% increase in the drag coefficient for the three pattern resolutions on average, compared to the corresponding ellipsoids with a smooth surface.

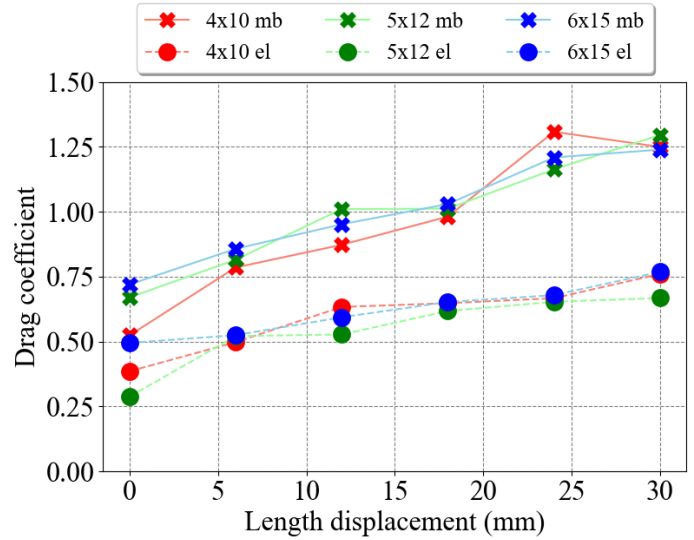


**FIGURE 9: COMPARISON OF DRAG COEFFICIENT.  $mb$ :=MAGIC BALL  $e/$ :=ELLIPSOID (MAXIMUM STANDARD DEVIATION IS 0.0175 FOR MAGIC BALLS, 0.0178 FOR ELLIPSOIDS)**

The complex surface geometry will disrupt the flow, making the boundary layer thicker and more turbulent. Besides, the complex surface can also generate vortexes and eddies. These effects can probably explain why the drag coefficient of magic balls is larger than that of the smooth ellipsoids.

The drag in this paper can be compared across the magic balls with different resolutions, since the area of PET sheets used to fabricate the scaled-down magic balls is kept to be constant and the aspect ratio of the sheets of the patterns is practically identical. In this case, the magic balls with different resolutions have similar geometry, and the main difference is the different numbers of waterbomb units. With an adequately increasing number of waterbomb units on each sheet, the size of each unit could become smaller and the magic ball will become more smooth. Since the patterns do not have a great number of units and the number of units does not vary dramatically across different pattern resolutions in this experiment, the effect of the smoothness on the drag coefficient cannot be obviously observed.

In this paper, the rigid standoffs are used in the drag characterization to adjust the length displacement of the scaled-down magic balls. In this case, the body length is strictly controlled, and the corresponding states of the real robot are represented. Nevertheless, since the flexible fishing line is used to hold the body length in the real robot, the length of the robot could slightly change, leading to a shape change of the robot when there are external disturbances. However, this effect could be negligible since the fishing line is flexible only within a very small strain range. Therefore, the scaled-down samples can effectively represent the real scenario of the robot.

Finally, the drag coefficient of the magic balls is large compared to that of the smooth ellipsoids and indicates that future versions of our robot may benefit from a smooth skin. The origami magic ball, which directly converts length change into volume change could remain a skeleton of the resulting robot. At the same time, however, other factors in addition to drag will

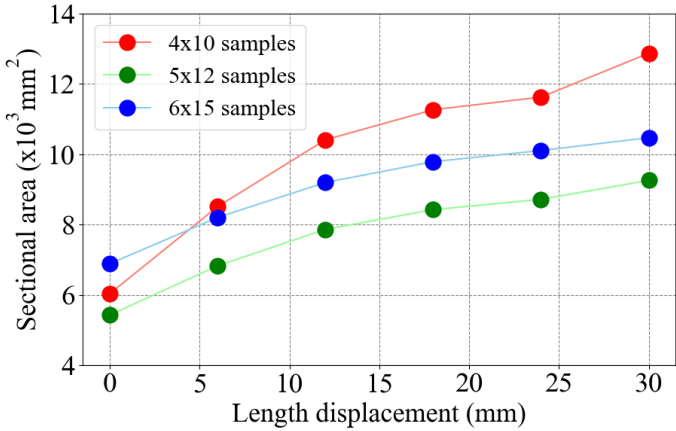


**FIGURE 10: COMPARISON OF SECTIONAL AREA OF BOTH MAGIC BALLS AND ELLIPSOIDS**

affect the energy efficiency and controllability of the robot. In particular, the compliance of the robot's body will have an effect on its thrust and its drag when it is in the water. As the robot is moving forward, the force from the surrounding water could play a role in squeezing the magic ball into different shapes. Thus, further exploration into other properties of the origami magic ball is required to truly optimize the robot design.

## 5. CONCLUSION

In this paper, the drag coefficients of three origami magic balls ( $4 \times 10$ ,  $5 \times 12$ , and  $6 \times 15$ ) in six states (compression length: 0 cm, 0.6 cm, 1.2 cm, 1.8 cm, 2.4 cm, and 3 cm) are experimentally determined. By comparing the drag and drag coefficient of the magic balls and their corresponding ellipsoids, the influence of the complex surface geometry of the magic balls is discovered. From the results, the variation of the drag coefficient of the magic balls with different resolutions in the same state is less than 37.3%. The complex surface geometry of the magic balls contributes to a 57%, 86%, and 61% increase in the drag coefficient as compared to the smooth ellipsoids. The variation of drag coefficient across different states could provide intuition for the future design optimization of the robot and the design of the control method. Of course, some limitations must be addressed before we can use these conclusions for future iterations of our underwater robot design. In this paper, the flow direction of fluid is set to be the same as the swimming direction of our robot, and the wind speed was set to be constant at approximately the robot's average velocity. However, in the real scenario, the attack angle could be non-zero, the robot is constantly accelerating and decelerating, and sometimes the flow could be turbulent. Therefore, it can be meaningful to characterize the drag coefficient with various attack angles and Reynolds numbers in the future.

## ACKNOWLEDGMENTS

Support for this project has been provided in part by NSF Grant No. 2121887, by ONR Award #N00014-23-1-2068, by the Pennsylvania Space Grant Consortium, and by the Penn Center for Undergraduate Research & Fellowships. We thank Sarah Ho,

Terence Lin, Razaq Aribidesi, Joe Valdez, and Jeremy Wang for their assistance with fabricating and assembling the load cell setup. We also thank Peter Bruno for providing us with access to the wind tunnel, and Erica Feehery for helping to set up load cell tests in the wind tunnel.

## REFERENCES

- [1] Noh, M., Kim, S.W., An, S., Koh, J.S. and Cho, K.J. "Flea-inspired catapult mechanism for miniature jumping robots." *IEEE Trans. Robotics* Vol. 28 No. 5 (2012): p. 1007–1018. DOI [10.1109/TRO.2012.2198510](https://doi.org/10.1109/TRO.2012.2198510).
- [2] Carlson, Jaimie, Friedman, Jason, Kim, Christopher and Sung, Cynthia. "REBOund: Untethered origami jumping robot with controllable jump height." *IEEE International Conference on Robotics and Automation (ICRA)*: pp. 10089–10095. 2020. DOI [10.1109/ICRA40945.2020.9196534](https://doi.org/10.1109/ICRA40945.2020.9196534).
- [3] Felton, S.M., Tolley, M.T., Onal, C.D., Rus, D. and Wood, R.J. "Robot self-assembly by folding: A printed inchworm robot." *2013 IEEE International Conference on Robotics and Automation*: pp. 277–282. Karlsruhe, Germany, May 6—10, 2013. DOI [10.1109/ICRA.2013.6630588](https://doi.org/10.1109/ICRA.2013.6630588).
- [4] Onal, C.D., Wood, R.J. and Rus, D. "Towards printable robotics: Origami-inspired planar fabrication of three-dimensional mechanisms." *2011 IEEE International Conf. on Robotics and Automation*: pp. 4608–4613. Shanghai, China, May 9—13, 2011. DOI [10.1109/ICRA.2011.5980139](https://doi.org/10.1109/ICRA.2011.5980139).
- [5] Rus, Daniela and Sung, Cynthia. "Spotlight on origami robots." *Science Robotics* Vol. 3 No. 15 (2018): p. eaat0938. DOI [10.1126/scirobotics.aat0938](https://doi.org/10.1126/scirobotics.aat0938).
- [6] Belke, C.H. and Paik, J. "Mori: A Modular Origami Robot." *IEEE/ASME Trans. Mechatronics* Vol. 22 No. 5 (2017): pp. 2153–2164. DOI [10.1109/TMECH.2017.2697310](https://doi.org/10.1109/TMECH.2017.2697310).
- [7] Chen, Y., Feng, H., Ma, J., Peng, R. and You, Z. "Symmetric waterbomb origami." *Proc.R.Soc.A* Vol. 472 No. 2190 (2016): 27436963. DOI [10.1098/rspa.2015.0846](https://doi.org/10.1098/rspa.2015.0846).
- [8] Lee, D.Y., Kim, J.S., Kim, S.R., Koh, J.S. and Cho, K.J. "The deformable wheel robot using magic ball origami structure." *Proceedings of the ASME 2013 International Design Engineering Technical Conferences and Computers and Information in Engineering Conference*. Portland, OR, August 4—7, 2013. DOI [10.1115/DETC2013-13016](https://doi.org/10.1115/DETC2013-13016).
- [9] Yang, Z., Chen, D., Levine, D.J. and Sung, C.R. "Origami-Inspired Robot That Swims via Jet Propulsion." *IEEE Robotics and Automation Letters* Vol. 6 No. 4 (2021): pp. 7145–7152. DOI [10.1109/LRA.2021.3097757](https://doi.org/10.1109/LRA.2021.3097757).
- [10] Onal, C.D., Wood, R.J. and Rus, D. "An origami-inspired approach to worm robots." *IEEE/ASME Trans. Mechatronics* Vol. 18 No. 2 (2013): pp. 430–438. DOI [10.1109/TMECH.2012.2210239](https://doi.org/10.1109/TMECH.2012.2210239).
- [11] Li, X., McWilliams, J., Li, M., Sung, C.R. and Jiang, C. "Soft Hybrid Aerial Vehicle via Bistable Mechanism." *2021 IEEE International Conference on Robotics and Automation (ICRA)*: pp. 7107–7113. Xi'an, China, May 30 – June 05, 2021. DOI [10.1109/ICRA48506.2021.9561434](https://doi.org/10.1109/ICRA48506.2021.9561434).

- [12] Chukewad, Y.M., James, J., Singh, A. and Fuller, S. “RoboFly: An Insect-Sized Robot With Simplified Fabrication That Is Capable of Flight, Ground, and Water Surface Locomotion.” *IEEE Transactions on Robotics* Vol. 37 No. 6 (2021): pp. 2025–2040. DOI [10.1109/TRO.2021.3075374](https://doi.org/10.1109/TRO.2021.3075374).
- [13] Gibouin, F., Raufaste, C., Bouret, Y. and Argentina, M. “Study of the thrust–drag balance with a swimming robotic fish.” *Physics of Fluids* (2018).
- [14] Hou, L., Zhang, L. and Kim, J. “Energy Modeling and Power Measurement for Mobile Robots.” *Energies* Vol. 12 No. 1:27 (2019). DOI [10.3390/en12010027](https://doi.org/10.3390/en12010027).
- [15] Zarebidoki, M. “The Effects of Air Drag Force on the Efficiency and Control of lightweight higher Speed Robotics.” *2021 27th International Conference on Mechatronics and Machine Vision in Practice (M2VIP)*: pp. 400–404. Shanghai, China, November 26—28, 2021. DOI [10.1109/M2VIP49856.2021.9665113](https://doi.org/10.1109/M2VIP49856.2021.9665113).
- [16] Zhang, J., Wang, C. and Yan, X. “Aerodynamic Drag Characteristics of Miura-Ori Composite Structure.” *J. Aerosp. Eng.* Vol. 34 No. 4 (2021): 06021004. DOI [10.1061/\(ASCE\)AS.1943-5525.0001273](https://doi.org/10.1061/(ASCE)AS.1943-5525.0001273).
- [17] Park, C.Y., Lee, Y.A., Jang, J. and Han, M.W. “Origami and Kirigami Structure for Impact Energy Absorption: Its Application to Drone Guards.” *Sensors (Basel)* Vol. 23 No. 4 (2023): 36850745. DOI [10.3390/s23042150](https://doi.org/10.3390/s23042150).
- [18] Cozmei, M., Hasseler, T., Kinyon, E., Wallace, R., Deleo, A.A. and Salviato, M. “Aerogami: Composite origami structures as active aerodynamic control.” *Composites Part B: Engineering* Vol. 184 (2020): p. 107719. DOI [10.1016/j.compositesb.2019.107719](https://doi.org/10.1016/j.compositesb.2019.107719).
- [19] Tolman, K.A., Crampton, E.B., Stucki, C.L., Maynes, D. and Howell, L.L. “Design of an Origami-Inspired Deployable Aerodynamic Locomotive Fairing.” *The Proceedings from the 7th International Meeting on Origami in Science, Mathematics, and Education*, Vol. 3: pp. 669–684. Oxford, UK, September 4–7, 2018.
- [20] Marzin, T., de Langre, E. and Ramananarivo, S. “Shape re-configuration through origami folding sets an upper limit on drag.” *Proc.R.Soc.A* Vol. 478 No. 2267 (2022): 20220592. DOI [10.1098/rspa.2022.0592](https://doi.org/10.1098/rspa.2022.0592).
- [21] Hall, N. “Drag Coefficient.” National Aeronautics and Space Administration (2022). Accessed July 28, 2022, URL <https://www1.grc.nasa.gov/beginners-guide-to-aeronautics/drag-coefficient/>.
- [22] Khader, M.H. Abdul. “Effects of wave drag on submerged bodies.” *La Houille Blanche* No. 8 (1979): pp. 465–470. DOI [10.1051/lhb/1979044](https://doi.org/10.1051/lhb/1979044).
- [23] Dwyer Instruments Inc. “Mark II Series Molded Plastic Manometers Specifications - Installation and Operating Instructions.” Mark II Model No.25 inclined-vertical manometer datasheet. May 2013.